An Analytical Model for Nonlinear-Elastic Compliant Mechanisms With Tension–Compression Asymmetry

Hargrove, Brianne; Frecker, Mary; Nastevska, Angela; Jovanova, Jovana

Important note
To cite this publication, please use the final published version (if applicable).
Please check the document version above.

An Analytical Model for Nonlinear-Elastic Compliant Mechanisms With Tension–Compression Asymmetry

Brianne Hargrove[1]
Department of Mechanical Engineering,
Penn State University,
University Park, PA 16802
e-mail: bbh5128@psu.edu

Mary Frecker
Department of Mechanical Engineering,
Penn State University,
University Park, PA 16802
e-mail: mxf36@psu.edu

Angela Nastevska
Kentaur-Impex,
Str. 516 No. 1,
Skopje 1000, North Macedonia
e-mail: angela.nastevska@kentaur.com.mk

Jovana Jovanova
Department of Mechanical Engineering,
Delft University of Technology,
Mekelweg 5,
Delft 2628 CD, The Netherlands
e-mail: j.jovanova@tudelft.nl

While nonlinear-elastic materials demonstrate potential in enhancing the performance of compliant mechanisms, their behavior still needs to be captured in a generalized mechanical model. To inform new designs and functionality of compliant mechanisms, a better understanding of nonlinear-elastic materials is necessary and, in particular, their mechanical properties that often differ in tension and compression. In the current work, a beam-based analytical model incorporating nonlinear-elastic material behavior is defined for a folding compliant mechanism geometry. Exact equations are derived capturing the nonlinear curvature profile and shift in the neutral axis due to the material asymmetry. The deflection and curvature profile are compared with finite element analysis along with stress distribution across the beam thickness. The analytical model is shown to be a good approximation of the behavior of nonlinear-elastic materials with tension–compression asymmetry under the assumptions of the von Kármán strain theory. Through a segmentation approach, the geometries of a semicircular arc and folding compliant mechanism design are defined. The deflection of the folding compliant mechanism due to an applied tip load is then evaluated against finite element analysis and experimental results. The generalized methods presented highlight the utility of the model for designing and predicting the behavior of other compliant mechanism geometries and different nonlinear-elastic materials.
[DOI: 10.1115/1.4065025]

Keywords: compliant mechanisms, shape memory alloys, superelasticity, hyperelasticity, tension–compression asymmetry, analytical model, additive manufacturing, folding and origami, mechanism design

1 Introduction

Compliant mechanisms (CMs) are highly flexible and monolithic structures that have applications in shape morphing, origami engineering, and energy storage. Nonlinear-elastic materials and shape memory alloys (SMAs) such as functionally graded Nitinol (NiTi) can improve the energy storage properties of CMs [1], but the behavior of such materials in CMs has not been well studied. As a disruptive technology, additive manufacturing (AM) has enabled the fabrication of lightweight, functional, and complex structures. Due to the design freedom that AM provides, research interest has grown in additively manufactured CMs.

Prior research has mostly focused on the performance of CMs driven by their design rather than by their mechanical properties. Early work was almost exclusively limited to CMs with material and geometric linearity [2–6]. Some researchers then expanded their models to account for large deformations through geometric

nonlinearity in the design of CMs with rigid sections connected by small-length flexural pivots [7], with large-displacement revolute or translational flexible joints [8], with semicircular beam hinges [9], and for different loading and boundary conditions such as combined end loads [10] as well as for cantilever, pinned-pinned, and fixed-guided CMs [11]. Geometric nonlinearity has also been introduced in the topology optimization and synthesis of CMs for large-displacement path-generation [12], self and mutual contact in the form of contact-aided compliant mechanisms [13], and multi-port and multi-material CMs with linear-elastic mechanical properties [14]. The problem of accounting for material nonlinearity has not been widely considered in the literature due to the modeling complexity. The main contribution of this paper is the consideration of both geometric and asymmetric material nonlinearity in CMs that can be approximated as elastic beams or combinations of beam segments. Geometric nonlinearity is a result of large deformations that cause the relationship between force and displacement to become nonlinear. Asymmetry is defined as the nonlinear-elastic material having unequal mechanical properties in tension and compression.

Finite element analysis (FEA) and topology optimization are common methods for designing and modeling CMs. For example, FEA was used to simulate variable stiffness in a parallel-guided

CM with pneumatic-actuated layer jamming [15], and topology optimization was used to design sports headgear liners with bioinspired compliant mechanism lattices [16]. Topology optimization was also used to obtain designs for CMs undergoing large deformations using a neo-Hookean or hyperelastic material model [17–19]. In some cases, material nonlinearity is implemented mainly to avoid local instabilities while solving the large-deformation optimization problem [18] as opposed to deliberately modeling a CM made with a nonlinear-elastic material.

Mechanical models using exact or semi-analytical solutions have been explored to overcome the computational cost of FEA-based methods. Howell and Midha developed a kinematic model to parameterize the deflection of flexible beams using the pseudo-rigid body model (PRBM), which accounts for large deformations but is limited to linear elasticity [20]. PRBMs have been applied to circular beams and bistable CMs under small deformations [21,22], and extended to large deformations using segmented models [23] or chained pseudo-rigid body models for curved beams [24].

Another type of analytical model is the beam-based model. Various techniques have been used to model flexible beams and CMs accounting for large deformations or geometric nonlinearity, such as nonlinear shooting and Adomian decomposition [25], chained beam-constraint-models [26], assumed mode methods [27], analog equation methods [28], and closed-form solutions [29–31]. More recent studies have also incorporated nonlinear-elastic materials such as that developed by Eshghinejad and Elahinia [32] for a superelastic NiTi beam undergoing small deformations, based on Auricchio's material model [33]. Our research group has extended this model to include large deformations [34] adapting an integral approach for initially straight and curved beams [35,36]. In this model, the tensile and compressive stresses in the beam were assumed to be symmetric. Yet, for additively manufactured CMs, the behavior of parts with anisotropic and asymmetric mechanical properties requires further investigation. Analytical models based on the superelastic NiTi beam model [32] were developed to include tension–compression asymmetry for superelastic cantilever beams with Timoshenko beam theory [37,38]. However, a generalized analytical model is still needed to handle various nonlinear-elastic materials and complex CM geometries. This work aims to incorporate the asymmetry of nonlinear-elastic materials into a CM model subject to large deformations, which is introduced next.

2 Methods

To consider CMs made from nonlinear-elastic materials, such as those used in AM, the addition of material nonlinearity is presented first. The focus of this section is to highlight the modeling of tension–compression asymmetry using a multilinear material model. This approach is ultimately applied to a folding CM design that was presented in previous work by our research group, where it was modeled as a compliant joint that could be used in large-scale foldable shipping containers [39]. The geometry of the folding CM is approximated using a chain of connected cantilever beams or segments.

2.1 Modeling Tension–Compression Asymmetry. For most nonlinear-elastic materials, the strain is assumed to vary linearly with the stress up to a critical point. Beyond this point, the material experiences changes in its response where the strain is no longer directly proportional to the stress even at infinitesimal strains [40,41]. This nonlinear-elastic behavior is captured through the development of a multilinear material model that is defined by several linear sections. The linear sections are represented by piecewise stress–strain equations that capture the change in the material response at a critical strain. The material model includes tension–compression asymmetry, i.e., the stress–strain behavior is not symmetric across the centroidal axis (CA) of a given geometry.

The material model is divided into k linear sections; in this case, three sections each in tension and compression. This approach is

adapted from Ref. [32] where the superelastic behavior of NiTi was defined by three piecewise equations. The nonlinear-elastic material is defined as follows: (1) a linear-elastic region, (2) a nonlinear-elastic region, and (3) a strain-hardening region. We approximate the nonlinear-elastic behavior with a corresponding multilinear model as shown in Fig. 1. The piecewise linear equations are given in Eq. (1), where the subscript "(t, c)" is replaced by either "t" for tension or "c" for compression. The subscript "*" represents a critical value of the strain or stress at which the elastic modulus changes, as indicated in Fig. 1. It is noted that only stress–strain equations for loading of the model are derived, and unloading is not considered.

$$
\sigma_k^{(t,c)} = \begin{cases} E_1^{(t,c)}\varepsilon & \text{if } |\varepsilon| < |\varepsilon_1^{(t,c)*}| \\ E_2^{(t,c)}\left(\varepsilon - \dfrac{\sigma_1^{(t,c)*}}{E_1^{(t,c)}}\right) + \sigma_1^{(t,c)*} & \text{if } |\varepsilon_1^{(t,c)}| < |\varepsilon| < |\varepsilon_2^{(t,c)*}| \\ E_3^{(t,c)}(\varepsilon - \varepsilon_{res}^{(t,c)}) & |\varepsilon| > |\varepsilon_2^{(t,c)*}| \end{cases}
$$

$$
\text{for} \quad k = 1, \ldots, 3
$$

$$
\text{where} \quad E_2^{(t,c)} = \frac{\sigma_2^{(t,c)*} - \sigma_1^{(t,c)*}}{\sigma_2^{(t,c)*}/E_3^{(t,c)} + \varepsilon_{res}^{(t,c)} - \sigma_1^{(t,c)*}/E_1^{(t,c)}}
$$

$$
\varepsilon_1^{(t,c)*} = \frac{\sigma_1^{(t,c)*}}{E_1^{(t,c)}} \quad \text{and} \quad \varepsilon_2^{(t,c)*} = \frac{\sigma_2^{(t,c)*}}{E_3^{(t,c)}} + \varepsilon_{res}^{(t,c)} \qquad (1)
$$

The constitutive equation for the strain (ε) in Ref. [32] stems from the Euler–Bernoulli hypothesis, which enforces small strains, small rotations, and small deflections. The assumptions of the Euler–Bernoulli theory are relaxed in the current work to include moderately large rotations and large deflections through the von Kármán strain formulation [42–44]. The normality condition is also relaxed to include the shear strain, according to Timoshenko beam theory [42]. It is noted that the von Kármán strains are still assumed to be small. However, it is not well documented in the literature what the threshold for small strain should be quantitatively, since the magnitude of the strain depends on the material and the geometry. Small strain and moderately large rotations, in this work, instead refer to assumptions made on the order of magnitude of the strain to remove the higher order terms defined in finite strain theory. For the von Kármán theory, the strain is assumed to be of order $O(\varepsilon)$ and the rotations are of $O(\varepsilon^{1/2})$ [45]. Large deformations result from a nonlinear relationship between force and deflection which is introduced in the definition of curvature.

The von Kármán strain includes a membrane component of the strain (ε_m), allowing for axial stretching. The axial strain is determined by relating the axial force caused by the applied loads, as in Ref. [31], to the integral of the axial stress. The bending component of the strain (ε_b) is instead proportional to the curvature (κ). The curvature is found by relating the moment caused by the applied loads, as described in Refs. [31,34], to the integral of the normal stress. Equation (2) gives the expression of the total strain, where the bending strain is substituted into Eq. (1). Given a beam, for example, the y position along the beam's thickness is denoted as y^* and y_o^* is the neutral axis shift. Equation (3) is the shear strain as defined in Ref. [31]. The axial and transverse deflections of a point along the centroidal axis of the beam are u and v, respectively.

$$
\varepsilon = \varepsilon_m + \varepsilon_b
$$

$$
\text{where} \quad \varepsilon_m = \frac{du}{dx} + \frac{1}{2}\left(\frac{dv}{dx}\right)^2 \quad \text{and} \quad \varepsilon_b = \kappa(y^* - y_o^*) \qquad (2)
$$

$$
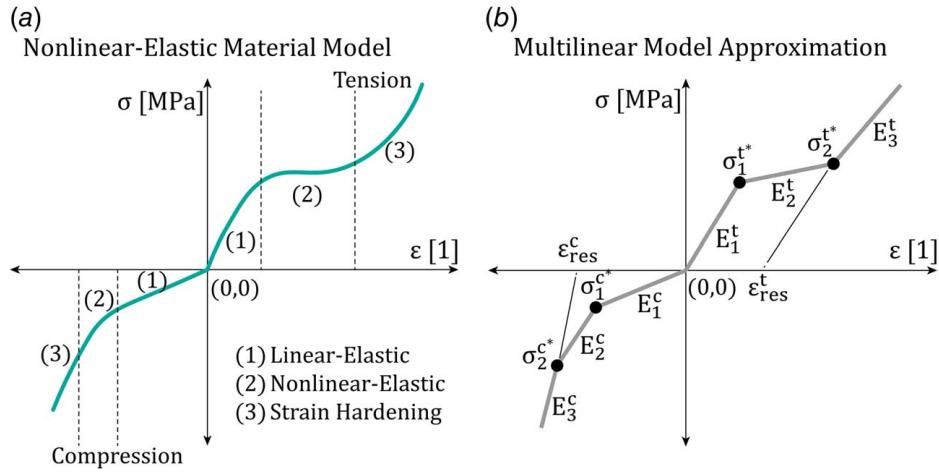\gamma_s = \frac{dv}{dx} - \sin\theta \qquad (3)
$$

Fig. 1 Example of a nonlinear-elastic material with asymmetric tensile and compressive mechanical properties (a) and its corresponding multilinear approximation defined by $k = 3$ linear sections (b)

In Fig. 1(b), the first linear section represents the initial linear-elastic response of the material up to critical stresses ($\sigma_1^{t^*}$, $\sigma_1^{c^*}$) and elastic moduli (E_1^t, E_1^c). The second section approximates the transition of the material response from linear-elastic to nonlinear-elastic by a change in the elastic moduli (E_2^t, E_2^c) up to critical stresses ($\sigma_2^{t^*}$, $\sigma_2^{c^*}$). Finally, the transition from nonlinear-elastic behavior to strain hardening in which the stress continues to rise with increasing strain is represented by another change in the elastic moduli (E_3^t, E_3^c) and the maximum residual strains are represented by ε_{res}^t and ε_{res}^c. Beyond this section, the stress is extrapolated for a given strain using the final values of the elastic moduli.

To incorporate material nonlinearity into a CM, the beam-based model is presented. The geometry of a CM is approximated by a chain of connected cantilever beams, which are referred to as segments. One segment is represented by either an initially straight or initially curved cantilever beam, as shown in Fig. 2, with non-follower axial and transverse loads (F_x, F_y) as well as a moment at the tip (M_o). The undeformed length of the initially straight beam is given by L and is deformed to its final position with projected length (l) and transverse tip deflection (m). In the case of the initially curved beam, it has an initial curvature of κ_o with a projected length of l_o and transverse tip deflection of m_o. Each segment has a uniform cross section with a thickness of $2b$ and a depth of a. The arc length (s) of the segment spans from 0 to the undeformed length (L).

The cantilever beam is discretized into five regions as shown in Fig. 3, for an initially straight beam. The parameter y_o^* tracks the shift in the neutral axis across the beam thickness ($2b$), while $y_1^{(t,c)^*}$ and $y_2^{(t,c)^*}$ are the critical points where the slope changes. The critical points across the beam thickness are determined using Eqs. (4) and (5).

$$y_1^{(t,c)^*} = y_o^* + \frac{\sigma_1^{(t,c)^*}}{E_1^{(t,c)}\kappa} \tag{4}$$

$$y_2^{(t,c)^*} = y_o^* + \frac{(\sigma_2^{(t,c)^*}/E_3^{(t,c)}) + \varepsilon_{res}^{(t,c)}}{\kappa} \tag{5}$$

The order in which the stress profile changes, either on the tensile or compressive side of the beam, is determined by the magnitudes
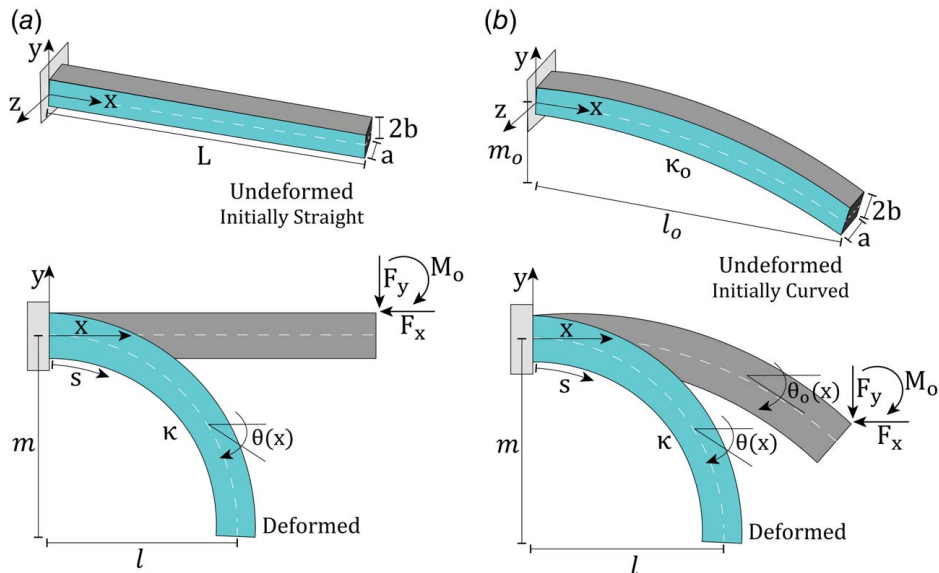

Fig. 2 Undeformed and deformed geometries of an initially straight cantilever beam (a) and an initially curved cantilever beam (b) subject to combined tip loading

of the critical stresses in tension relative to those in compression. The asymmetric stress profile also causes the neutral axis to shift in order to maintain a state of equilibrium. For example, the neutral axis shifts with respect to the centroidal axis (CA) toward the direction of the highest stress. As shown in Fig. 3, the neutral axis shifts upward when the tensile stresses are higher and downward when the compressive stresses are higher.

To determine the internal force and the moment due to bending in each region, the stress ($\sigma_k^{(t,c)}$) is integrated across the beam thickness ($2b$). The bending strain (ε_b) in Eq. (2) is substituted into the expressions of the stress to introduce the curvature (κ). For example, Eq. (6) defines the internal force and moment in the fifth region of the beam (F_5, M_5). The force and moment are calculated in any region of the beam by deriving the corresponding integral equations described available in the Supplemental Materials on the ASME Digital Collection. The axial and shear forces (N_5, V_5) are defined similarly using the membrane and shear strains in Eq. (7), where k_s is the shear factor, ν is Poisson's ratio, and $G_k^{(t,c)}$ are the shear moduli.

$$F_5 = a\left[\int_{y_2^*}^{b}\sigma_3^t dy^* + \int_{y_1^*}^{y_2^*}\sigma_2^t dy^* + \int_{y_o^*}^{y_1^*}\sigma_1^t dy^* + \int_{y_1^{c*}}^{y_o^*}\sigma_1^c dy^* \right.$$
$$\left. + \int_{y_2^{c*}}^{y_1^{c*}}\sigma_2^c dy^* + \int_{-b}^{y_2^{c*}}\sigma_3^c dy^* \right]$$

$$M_5 = \begin{aligned}a&\left[\int_{y_2^*}^{b} y^*\sigma_3^t dy^* + \int_{y_1^*}^{y_2^*} y^*\sigma_2^t dy^* + \int_{y_o^*}^{y_1^*} y^*\sigma_1^t dy^*\right.\\&\left.+ \int_{y_1^{c*}}^{y_o^*} y^*\sigma_1^c dy^* + \int_{y_2^{c*}}^{y_1^{c*}} y^*\sigma_2^c dy^* + \int_{-b}^{y_2^{c*}} y^*\sigma_3^c dy^* \right]\end{aligned}$$ (6)

$$N_5 = \begin{aligned}a&\left[\int_{y_2^t}^{b} E_3^t\varepsilon_m dy^* + \int_{y_1^t}^{y_2^t} E_2^t\varepsilon_m dy^* + \int_{y_o^*}^{y_1^t} E_1^t\varepsilon_m dy^*\right.\\&\left.+ \int_{y_1^c}^{y_o^*} E_1^c\varepsilon_m dy^* + \int_{y_2^c}^{y_1^c} E_2^c\varepsilon_m dy^* + \int_{-b}^{y_2^c} E_3^c\varepsilon_m dy^* \right]\end{aligned}$$

$$V_5 = \begin{aligned}ak_s&\left[\int_{y_2^t}^{b} G_3^t\gamma_s dy^* + \int_{y_1^t}^{y_2^t} G_2^t\gamma_s dy^* + \int_{y_o^*}^{y_1^t} G_1^t\gamma_s dy^*\right.\\&\left.+ \int_{y_1^c}^{y_o^*} G_1^c\gamma_s dy^* + \int_{y_2^c}^{y_1^c} G_2^c\gamma_s dy^* + \int_{-b}^{y_2^c} G_3^c\gamma_s dy^* \right]\end{aligned}$$

where

$$k_s = \frac{10(1+\nu)}{12+11\nu} \quad \text{and} \quad G_k^{(t,c)} = \frac{E_k^{(t,c)}}{2(1+\nu)} \quad \text{for} \quad k = 1,\ldots,3 \quad (7)$$

The integration was performed symbolically in MATLAB to derive expressions of the curvature in each region of the beam. The general expression of the curvature is derived by multiplying the moment equilibrium equation by κ^2 to obtain the cubic polynomial equation in Eq. (8), and solving for κ. The internal moment in the beam is represented by M_{int} while the external moment caused by a set of applied loads to the beam tip is M_{BC}. The coefficients (A_M, B_M, C_M, D_M) are extracted from the symbolic expression of the curvature for each region of the beam and are available in the Supplemental Materials.

$$M_{int}(\kappa)^2 = A_M(\kappa)^3 + B_M(\kappa)^2 + C_M(\kappa) + D_M = M_{BC}^2(\kappa)^2$$

where

$$\kappa = \left(\sqrt{\left(\frac{D_M}{2A_M} + \frac{(B_M - M_{BC})^3}{27A_M^3} - \frac{C_M(B_M - M_{BC})}{6A_M^2}\right)^2 + \left(\frac{C_M}{3A_M} - \frac{(B_M - M_{BC})^2}{9A_M^2}\right)^3} - \frac{(B_M - M_{BC})^3}{27A_M^3} - \frac{D_M}{2A_M} + \frac{C_M(B_M - M_{BC})}{6A_M^2}\right)^{1/3}$$
$$- \frac{\frac{C_M}{3A_M} - \frac{(B_M - M_{BC})^2}{9A_M^2}}{\left(\sqrt{\left(\frac{D_M}{2A_M} + \frac{(B_M - M_{BC})^3}{27A_M^3} - \frac{C_M(B_M - M_{BC})}{6A_M^2}\right)^2 + \left(\frac{C_M}{3A_M} - \frac{(B_M - M_{BC})^2}{9A_M^2}\right)^3} - \frac{(B_M - M_{BC})^3}{27A_M^3} - \frac{D_M}{2A_M} + \frac{C_M(B_M - M_{BC})}{6A_M^2}\right)^{1/3}} - \frac{B_M - M_{BC}}{3A_M}$$ (8)

The critical curvatures between each region are determined using Eqs. (9) and (10). For an initially curved beam, the initial curvature (κ_o) is added to the curvature expression in Eq. (8) and to the expressions of the critical curvatures.

$$\kappa_1^{(t,c)} = \frac{\sigma_1^{(t,c)*}}{E_1^{(t,c)}(\pm b - y_o^*)}$$ (9)

$$\kappa_2^{(t,c)} = \frac{(\sigma_2^{(t,c)*}/E_3^{(t,c)}) + \varepsilon_{res}^{(t,c)}}{(\pm b - y_o^*)}$$ (10)

Since the analytical model incorporates a nonlinear-elastic material model with unequal tensile and compressive mechanical properties, the beam undergoes bending that is not symmetric. In other words, the neutral axis does not coincide with the centroidal axis of the beam ($y_o^* \neq 0$). The shift in the position of the neutral axis (y_o^*) for an asymmetric material is instead found from setting the internal force to zero. The computation of the integral equations was also done symbolically, and the solution was rearranged to solve

for y_o^*. In Eq. (11), the internal force equation ($F_{int} = 0$) is multiplied by y_o^{*2} such that the neutral axis can be solved for from the quadratic expression. Similar to the curvature equation, explicit expressions for the coefficients (A_F, B_F, C_F, D_F) are available in the Supplemental Materials on the ASME Digital Collection.

$$F_{int}(y_o^*)^2 = B_F(y_o^*)^2 + C_F(y_o^*) + D_F = 0$$

where

$$y_o^* = -\frac{C_F + \sqrt{C_F^2 - 4B_F D_F}}{2B_F}$$ (11)

With the presented analytical solutions, characterization of the asymmetric material nonlinearity is illustrated along a nonlinear-elastic cantilever beam. By extension, if the beam represents one segment of a CM design, material nonlinearity can be captured throughout the more complex geometry. The following section describes how the curvature is used in calculating the deflection of a single CM segment.
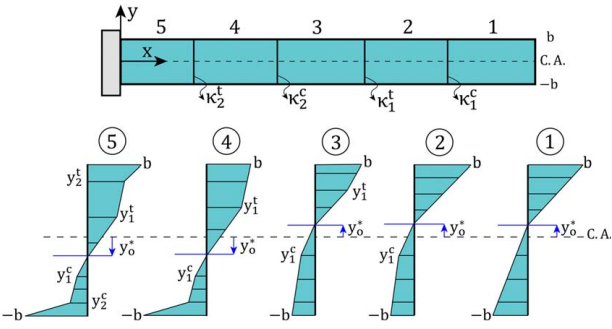
Fig. 3 Example of the discretized cantilever beam divided into five regions, for a generic nonlinear-elastic material, with the stress profile at specific critical curvatures and the shift in the neutral axis (y_o^*) from the CA

2.2 Beam-Based Model for Large Deformations. The curvature (κ) is central to defining the deflection since the curvature along the segment is not constant for combined loading conditions. It is necessary to account for not only pure bending due to an applied moment but also bending due to axial and transverse loads. The curvature is defined in Eq. (12).

$$\kappa = \frac{d\theta}{ds} = \frac{d^2y/dx^2}{[1 + (dy/dx)^2]^{3/2}} \qquad (12)$$

Per this equation, the curvature is defined as the rate of change of the slope (θ) with respect to the arc length. The value of the curvature is found from solving the equilibrium equation (Eq. (8)). By adapting an integral approach for cantilever beams undergoing large deformations, the slope is derived by taking the integral of the curvature. Given the geometric relationships illustrated in Fig. 4, for a differential element, it is found that $\sin(\theta)$ is equal to the integral of the curvature [35]. By rearranging this relationship, the slope is expressed as Eq. (13), which is integrated from 0 to L. This distance is represented by the arc length (s), which is equal to L at the tip of the deformed beam, i.e., $s(l) = L$.

$$\theta = \sin^{-1}\left(\int \kappa\, ds\right) \qquad (13)$$

Each beam segment is discretized into $N_p - 1$ differential elements. This allows for the definition of the slope for the ith element in Eq. (14). This equation assumes that for a large value of N_p, or a large number of discretization points, the curvature (κ_{i-1}) is a constant value within each differential element.

$$\theta_i = \theta_{i-1} + \sin^{-1}\left[\kappa_{i-1}(s_i - s_{i-1})\right] \qquad (14)$$
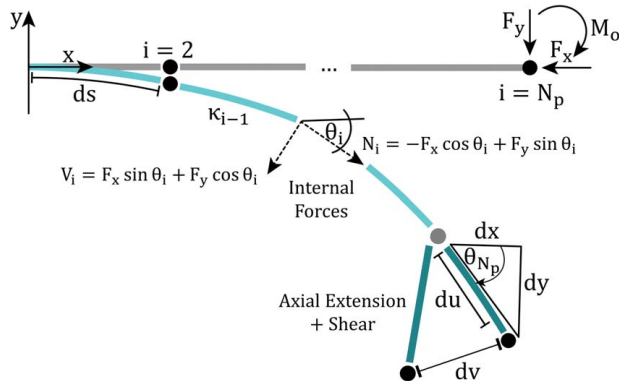

Fig. 4 Discretization of segment into N_p points from $i = 1$ to $N_p - 1$ elements

The x and y positions of each differential element, due to bending, are also related to the integral of the curvature. The expression of the curvature is decomposed as described in Refs. [7,11] for large deflection analysis. The axial and transverse displacements (u, v) are calculated separately from the displacements due to bending. The axial and shear force expressions in Eq. (7) are rearranged to solve for u and v, where N and V are shown to be a function of the tip loads (F_x, F_y) and the slope in Fig. 4. In the discretized form, the final x and y positions are Eqs. (15) and (16):

$$x_i = x_{i-1} + \frac{1}{\kappa_{i-1}}[\sin(\theta_i) - \sin(\theta_{i-1})] + (u_i - u_{i-1})\cos(\theta_i - \theta_{i-1})$$
$$+ (v_i - v_{i-1})\sin(\theta_i - \theta_{i-1}) \qquad (15)$$

$$y_i = y_{i-1} + \frac{1}{\kappa_{i-1}}[\cos(\theta_{i-1}) - \cos(\theta_i)] + (u_i - u_{i-1})\sin(\theta_i - \theta_{i-1})$$
$$- (v_i - v_{i-1})\cos(\theta_i - \theta_{i-1}) \qquad (16)$$

This formulation is for a segment modeled as an initially straight cantilever beam. For an initially curved beam, a constant curvature of $\kappa_o = 1/R_o$ is prescribed, where R_o is the initial radius of curvature. Following the same derivation in Eq. (14) and Eqs. (15) and (16), the initial slope (θ_o) and the initial x and y position of the initially curved beam are found by substituting κ_{i-1} with the initial curvature (κ_o). In this case, the initial curvature is known but the final curvature (κ) in the deformed configuration still needs to be solved. Once the curvature and deflection of a single segment are determined, the same procedure is used to approximate the behavior of a chain of beams or segments that make up two geometries: (1) a semicircular arc and (2) a folding CM.

2.2.1 Segmented Model for a Semicircular Arc. An analytical model using a segmented PRBM, where a semicircular arc was represented by a connection of rigid links and torsional springs, was shown to accurately predict the tip deflection of the arc compared to FEA [23]. Another approach was introduced where the arc was segmented into a chain of cantilever beams [34], which is explored further in this work. A semicircular arc with radius to the centroidal axis (R_c) and cross section ($a \times 2b$) is deformed by a combination of applied loads (F_x, F_y) and a moment (M_o) at its tip. The arc has a projected length l and transverse tip deflection m in its deformed position as shown in Fig. 5. To model the deflection, the arc is segmented into a chain of connected cantilever beams that can be either initially straight or initially curved. The model allows for connections of solely initially straight beams, solely initially curved beams, as well as a mixture of both types. The details of the segmentation approach are clarified and available in the Supplemental
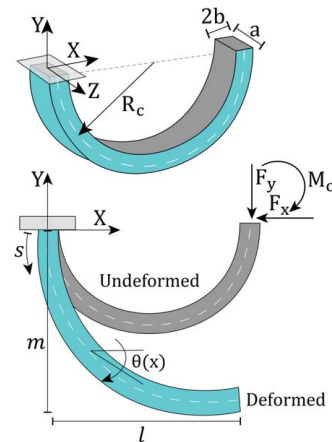

Fig. 5 Undeformed and deformed geometry of a semicircular arc subject to combined tip loading
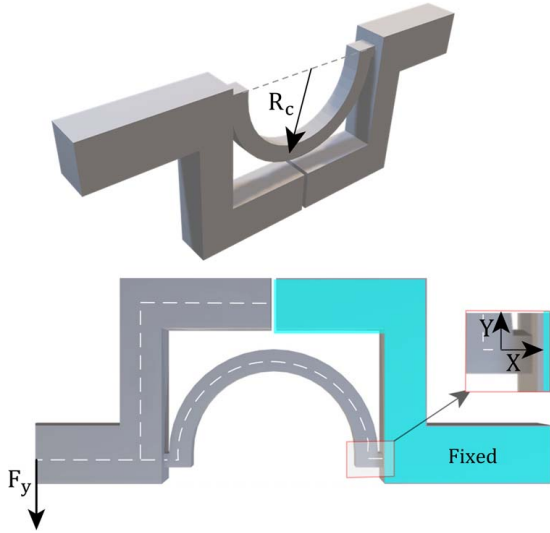
Fig. 6 Undeformed geometry of a folding CM subject to a transverse tip load, where the leftmost frame of the CM is fixed, and the CM deforms along a virtual neutral axis

Materials on the ASME Digital Collection. This approach is used to inform a similar segmented model for the folding CM design.

2.2.2 Segmented Model for a Folding Compliant Mechanism. While the folding CM and semicircular arc are similar in design, the boundary conditions for the folding CM differ. The CM geometry is presented in Fig. 6 and consists of a semicircular arc with small flexures on each end connected to two identical frames. The model is subject to a transverse load (F_y) at the tip of the CM. The boundary conditions for the folding CM design are based on the experimental setup in Ref. [23], the details of which are described in full. The folding CM geometry is also approximated using segmentation, such that the segmented model begins at the leftmost flexure. While the changes in the out-of-plane thickness (a) in the CM are neglected, given that the frames are considered rigid relative to the rest of the geometry, the model does account for the changes in the in-plane thickness ($2b$) and the length (L_s). These two parameters are estimated by discretizing each region of the CM into a chain of cantilever beams. The neutral axis of each beam aligns with the white dotted lines shown in Fig. 6. A new segment is defined following a change in direction, thickness, or length of each beam. The resulting segmented model is illustrated in Fig. 7.

This section concludes the methods for incorporating geometric nonlinearity into the analytical model. The analytical model is evaluated against FEA for two nonlinear-elastic materials: (1) superelastic NiTi and (2) hyperelastic thermoplastic polyurethane (TPU).
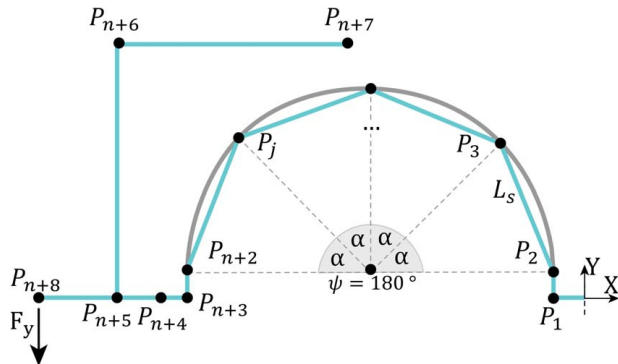

Fig. 7 Approximation of a folding CM subject to a transverse tip load using a segmented beam-based model

Table 1 Mechanical properties for the NiTi material model

Elastic moduli	Tension (GPa)	Compression (GPa)
E_1	69.2	50.0
E_2	72.9	82.7
E_3	71.4	72.7

2.3 Case Studies. Multilinear models are defined for superelastic NiTi and hyperelastic TPU, accounting for unequal mechanical properties in tension and compression. The behavior of superelastic NiTi with symmetric mechanical properties, for example, was characterized in three distinct regions along the cantilever beam [34]. However, for the asymmetric material model, five regions are needed to account for the five changes in the stress profile along the beam as shown in Fig. 3. This approach is also used in the derivation of the multilinear material model of TPU, accounting for the difference in mechanical properties.

2.3.1 Superelastic Nitinol (NiTi). SMAs, such as NiTi, have the unique properties of superelasticity (SE) and the shape memory effect (SME). Through a stress-induced phase transformation, SMAs can recover large amounts of elastic deformation. The SME, instead, is observed through a temperature-induced phase transformation in which a deformed SMA is heated and returns to its original state prior to being deformed. This case study looks only at SE of NiTi, under the assumption of constant temperature.

The multilinear model for NiTi uses the same mechanical properties in tension, such as the critical stresses ($\sigma_{1,2}^t$) and elastic moduli (E_k^t), as in Ref. [23], for the segmented PRBM approach. However, the original model is changed in the current work to include asymmetry by adjusting the mechanical properties in compression ($\sigma_{1,2}^{c*}$ and E_k^c). The elastic moduli in each linear section are given in Table 1, where the elastic modulus of the second linear section is calculated using Eq. (1). Figure 8 illustrates the multilinear material model for NiTi and the values of the stresses at each critical point. The critical points represent the locations where the stress profile changes, reflecting the nonlinear-elastic response of the material.

2.3.2 Thermoplastic Polyurethane. Rubber-like filaments used in polymer AM, such as thermoplastics, are elastomeric materials that exhibit hyperelasticity. Parts made from these filaments can
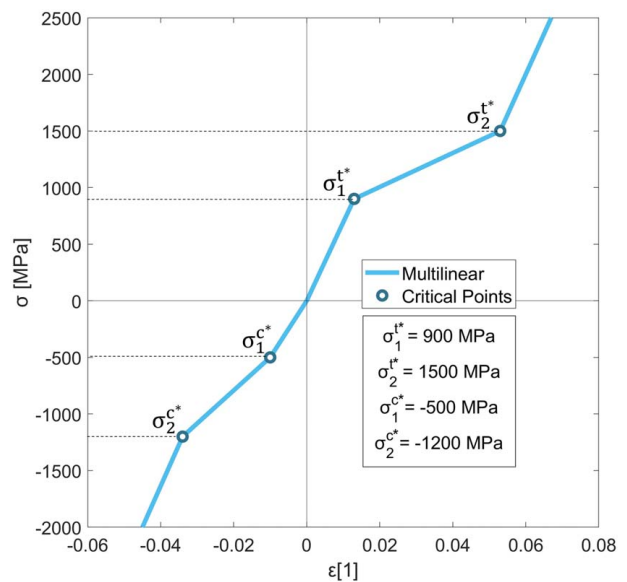

Fig. 8 Multilinear material model for NiTi with three linear sections and its corresponding critical stress values
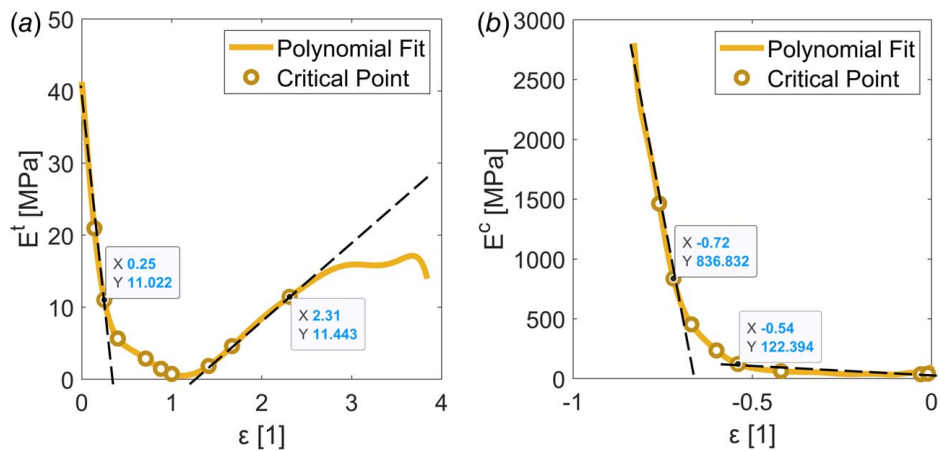
Fig. 9 Determination of the critical points of the multilinear model at the location of nonlinearity in the curve of the elastic modulus versus the strain in tension (a) and in compression (b)

achieve large changes in their shape while maintaining a constant volume, which is known as near-incompressibility. An example of such a filament is TPU. Due to its availability commercially with different values of shore hardness, TPU has been shown to be a versatile material. It has application in flexible systems such as soft robotics, as well as in systems in the medical and automotive industries that require hard, durable rubbers [46]. Since TPU has a more pronounced tension–compression asymmetry compared to the asymmetric NiTi material model presented, the following explores the approximation of TPU using the same multilinear model approach.

Published uniaxial test data for TPU with 95A shore hardness [47] were used for the material model. To derive the multilinear model, the data are discretized using three linear sections in tension and compression. First, the data are separated into the tensile and compressive data points, and each are fitted separately with a 15th order polynomial. The polynomial degree was studied at different values to achieve the best fit to the raw data and the highest R^2 value greater than 0.9. The R^2 value using a degree of 15 is 0.977 for the tensile data and 0.996 for the compressive data, which gives the best fit. Beyond a degree of 15, there is relatively minimal improvement in the R^2 error. The derivative of the polynomial equations is taken with respect to the strain to arrive at the slope of the curves, which is the change in elastic modulus. The approach developed in Ref. [23] is used to determine the location of the critical points and is summarized here.

When the percent difference in the change in the elastic modulus exceeds a target percentage of 50%, this marks the location of a critical point. Each section in tension and compression is approximated with three linear sections, resulting in four critical points total. A critical point is selected along the black dashed line, which is drawn along the relatively straight regions of the polynomial curve fit. The critical points are chosen such that the R^2 value of the multilinear model with respect to the uniaxial data is greater than 0.9. With the points shown in Fig. 9, the R^2 value is 0.992.

Using these four critical points, the elastic moduli in each linear section can be defined as in Table 2. In Fig. 10, the multilinear material model for TPU and the values of the stresses at each critical point are shown. The material models for NiTi and TPU presented are used in the following case studies comparing the analytical model with FEA and an experimental study, only for TPU.

2.3.3 Assumptions. The assumptions made for the analytical model are summarized as follows:

- Large deflections (geometric nonlinearity), but small strains and moderately large rotations using von Kármán strain theory.
- In-plane bending and stretching (only $\sigma_{xx} \neq 0$), but no out-of-plane behavior.
- The Poisson's ratio is zero ($\nu = 0$), i.e., no Poisson's effect.
- The CM is made from a nonlinear-elastic material (material nonlinearity).
- The neutral axis of the geometry does not coincide with the centroidal axis (asymmetric tension and compression).
- Hysteresis, creep, stress relaxation, and other time-dependent effects are not considered.

2.3.4 Finite Element Analysis. To validate the analytical models, COMSOL MULTIPHYSICS is used to run 2D FEA simulations of a (1) cantilever beam made from NiTi, (2) a semicircular arc made from TPU, and (3) the folding CM design made from TPU. The structural/solid mechanics module calculates the stresses,

Table 2 Mechanical properties for the TPU material model

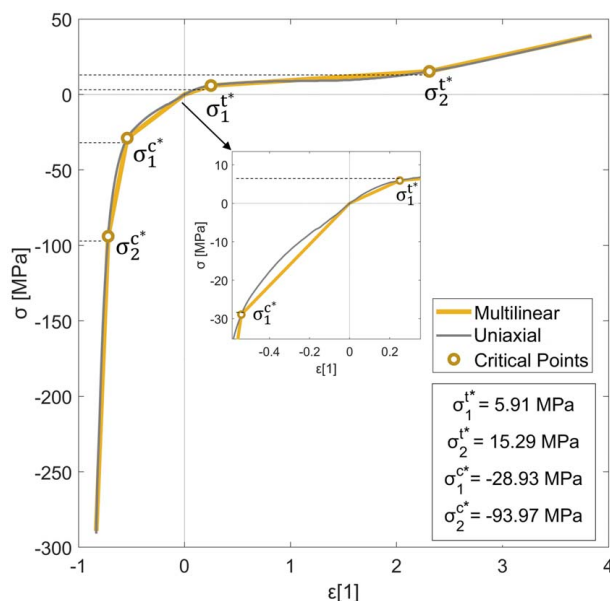| Elastic moduli	Tension (MPa)	Compression (MPa)
E_1	23.6	53.6
E_2	4.55	495.9
E_3	15.3	2090.6

Fig. 10 Multilinear material model for TPU with three linear sections and its corresponding critical stress values extracted from the original uniaxial data

Table 3 Geometry and loading applied to NiTi beam

Parameter	Value
L	200 mm
a	50 mm
b	5 mm
$F_{y,\max}$	−33 kN

Table 4 Geometry and loading of the TPU arc

Parameter	Value
R_c	17 mm
a	4 mm
b	2 mm
$F_{y,\max}$	−2 N

strains, and displacements of the geometry. Using this module, both a nonlinear-elastic material model and geometric nonlinearity are included. For NiTi, the multilinear material model data in Fig. 8 are imported into COMSOL as an interpolation function. For TPU, both the uniaxial data and its corresponding multilinear model in Fig. 10 are studied and the results for each are compared.

An extremely fine mapped mesh is used for the cantilever beam model with geometry listed in Table 3, with a minimum element size of 4×10^{-6} m and a maximum size of 2×10^{-3} m. The semicircular arc model with geometry listed in Table 4 has an extra fine free triangular mesh, with a minimum element size of 4.5×10^{-6} m and a maximum of 1.2×10^{-3} m. The same mesh type is used for the folding CM. All FEA simulations are evaluated across an auxiliary sweep. The applied loads (F_x, F_y, M_o) are ramped from zero up to their maximum values after $N_{\text{iter}} = 500$ iterations. In accordance with the analytical model, the Poisson's ratio (ν) is set to zero in the simulations such that a direct comparison can be made.

The results reported for the cantilever beam and semicircular arc cases are the deflection and curvature profiles in the deformed state, as well as the stress distribution along the fixed end. For the folding CM, the position of the final deformed shape is extracted along with

the deflection of the three tracked points (A, B, C) to compare against the experimental study. The accuracy of the analytical model is validated against FEA and experimental results in Sec. 3.

3 Results and Discussion

3.1 Cantilever Beam With NiTi. The cantilever beam shown is subject to a transverse load ($F_{y,\max}$) at its tip. The geometry of the beam and the loading condition is given in Table 3. The number of discretization points, N_p, is set to 5000 points. The deflection profile of the beam is plotted at five different iterations in Fig. 11(a), which represents the load steps up to the final value of $F_{y,\max}$. The ability of the analytical model to capture the force-deflection behavior of the beam is emphasized by its good agreement with the FEA model. The calculated mean-squared error (MSE) between the deflection curves of the two models is 1.83×10^{-8} m^2.

Figure 11(b) shows the curvature profile along the beam for the analytical and FEA models, which reflects the nonlinear behavior of the material upon reaching a critical curvature: $\kappa_1^c = 1.85$ m^{-1}, $\kappa_1^t = 2.87$ m^{-1}, $\kappa_c^2 = 6.36$ m^{-1}, and $\kappa_2^t = 10.40$ m^{-1}. The deflection and curvature profiles are normalized by the undeformed length of the beam (L). The stress profile along the beam thickness (y^*) at the fixed end is also plotted in Fig. 11(c) and compared with the Second Piola-Kirchhoff stress in FEA. The differences in the neutral axis position are also shown.

For NiTi and the current geometry, the model goes up to a maximum force of −33 kN. This corresponds to a maximum strain of 9.4% at the top fixed end of the beam. Beyond this strain, the practicality of the analytical model is limited due to non-convergence. NiTi is reported to exhibit up to 10% recoverable strain [48], which is on par with the maximum strain found for this example.

The accuracy of the analytical model is also demonstrated for a combined load case, where the same cantilever beam is subject to both an axial and transverse load (F_x, F_y). To illustrate the effect of including tension–compression asymmetry, Fig. 12 compares the beam deflection, curvature, and stress distribution using symmetric (S) and asymmetric (A) material models for NiTi. For the symmetric model, the compressive moduli and critical stresses are set equal to those in tension, i.e., $E_k^c = E_k^t$ and $\sigma_{1,2}^{c*} = -\sigma_{1,2}^{t*}$.
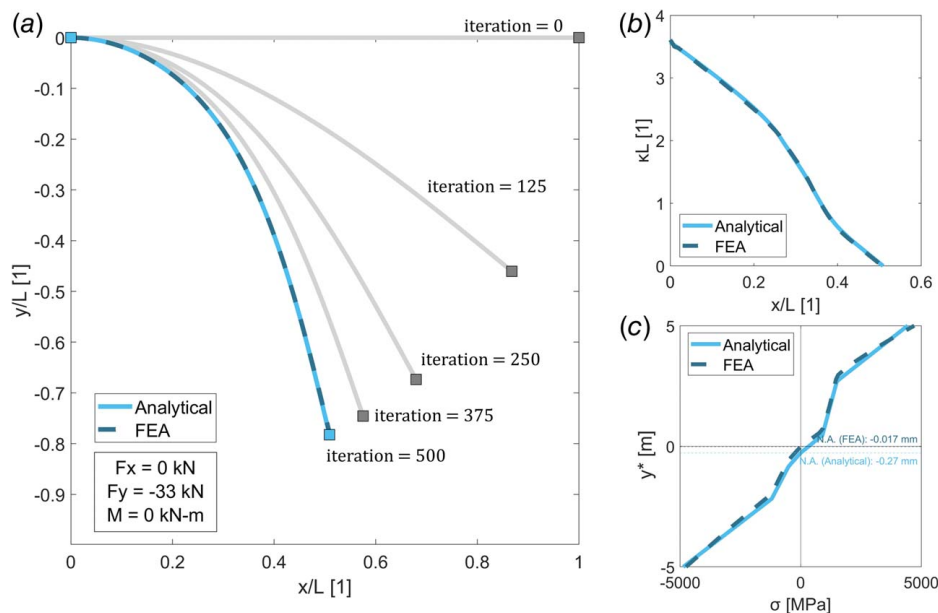

Fig. 11 Deflection profile of the NiTi analytical model subject to a transverse force of −33 kN showing the deflection history up to $N_{\text{iter}} = 500$ (a), curvature profile along the beam in its deformed position (b), and stress distribution and neutral axis position (c)
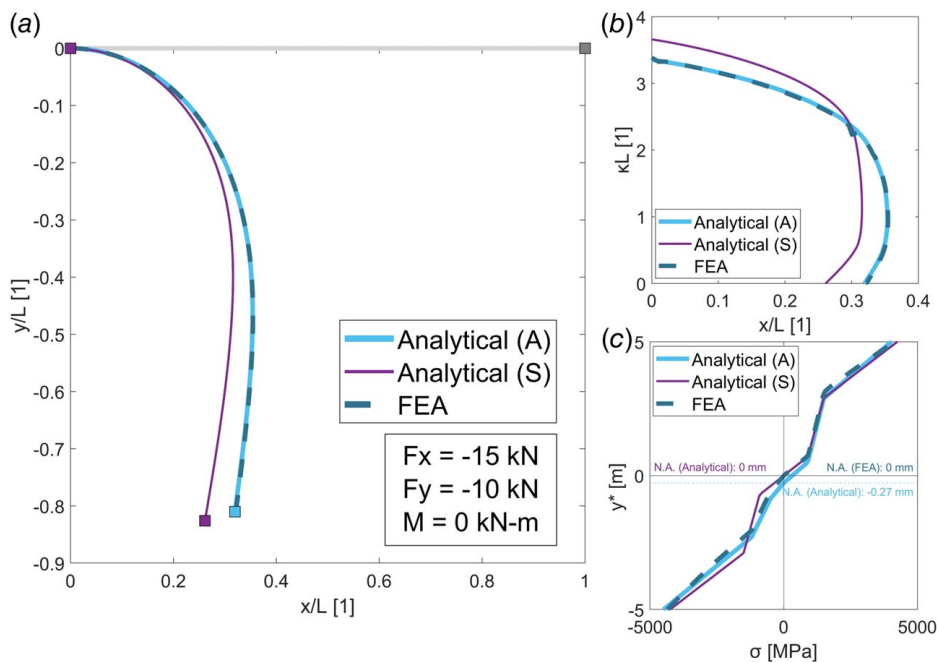
Fig. 12 Deflection of the NiTi beam for an axial force of −15 kN and transverse force of −10 kN (a), curvature profile (b), and stress distribution at the fixed end compared with FEA for the asymmetric A and symmetric S material models (c)

Even though the results of the symmetric model are close in shape to that of the FEA model, the symmetric model overpredicts the deflection and curvature profiles of the beam. The agreement of the model with FEA is thus improved with the addition of tension–compression asymmetry, as the MSE between the deflection curves decreases from 7.99×10^{-6} m^2 to 2.23×10^{-9} m^2. To explore the impact of a more pronounced asymmetry on the model accuracy, the force-deflection behavior of the segmented arc and folding CM design made from TPU is presented next.

3.2 Semicircular Arc With Thermoplastic Polyurethane.
The semicircular arc is segmented into $n = 20$ identical segments, with the simplest case being represented by initially straight cantilever beams. A segmented model consisting of initially curved beams or a heterogeneous combination can be selected to obtain similar results as those shown. Previous work has determined that the accuracy of the segmented model approach improves as the number of segments is increased [23]. Larger values of $n > 20$ have not shown notable differences in the results for the current model.

The undeformed geometry of the segmented arc is illustrated in Fig. 13 and is normalized by the undeformed diameter of the arc (D_c). The arc is subject to a transverse tip load ($F_{y,\max}$) and is defined by the parameters given in Table 4. The applied force of -2 N corresponds to a maximum strain of 12.4% in magnitude. As a result, the model is applicable for strains within the range corresponding to critical stresses $\sigma_1^{c^*}$ and $\sigma_1^{t^*}$ in Fig. 10 for this geometry.

The deflection of the arc is evaluated against the uniaxial data and its multilinear approximation in FEA. At a certain level of deformation, the analytical model begins to deviate from the FEA model using the uniaxial data (MSE $= 3.61 \times 10^{-6}$ m^2) but agrees well with the multilinear model as expected (MSE $= 2.98 \times 10^{-7}$ m^2) in Fig. 14(a). This finding is assumed to be a result of the selection of the critical points in the multilinear approximation. The curvature profile of the analytical model, and numerically meaningful results from the FEA model, are shown and normalized by the initial curvature (κ_o) in Fig. 14(b). The stress distribution at the fixed end of the arc, in Fig. 14(c), also illustrates that the second Piola-Kirchhoff

stress distribution across the neutral axis is not as asymmetric for the uniaxial data as it is for the multilinear case. This is assumed to be the reason for the differences seen in the deflection profiles between the two.

Between the critical stresses ($\sigma_1^{c^*}$ and $\sigma_1^{t^*}$), in Fig. 10, the curves of the TPU material model are approximated by one linear section each for tension and compression. If the location of the critical points is adjusted, or if the number of critical points in this region is increased, more of the nonlinearities in the material model could be captured and the agreement between the three curves could be improved. Additionally, the piecewise equations for the stress and strain (Eq. (13)) would also need to be derived for $k > 3$ linear sections.
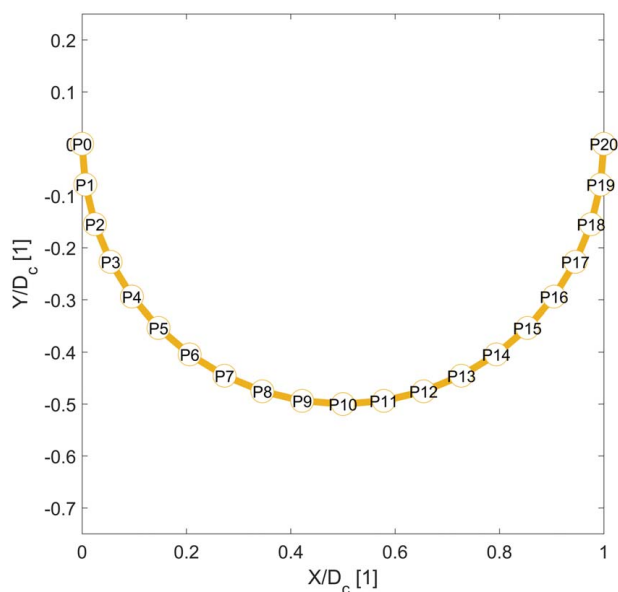

Fig. 13 Undeformed geometry of the segmented semicircular arc for $n = 20$ segments
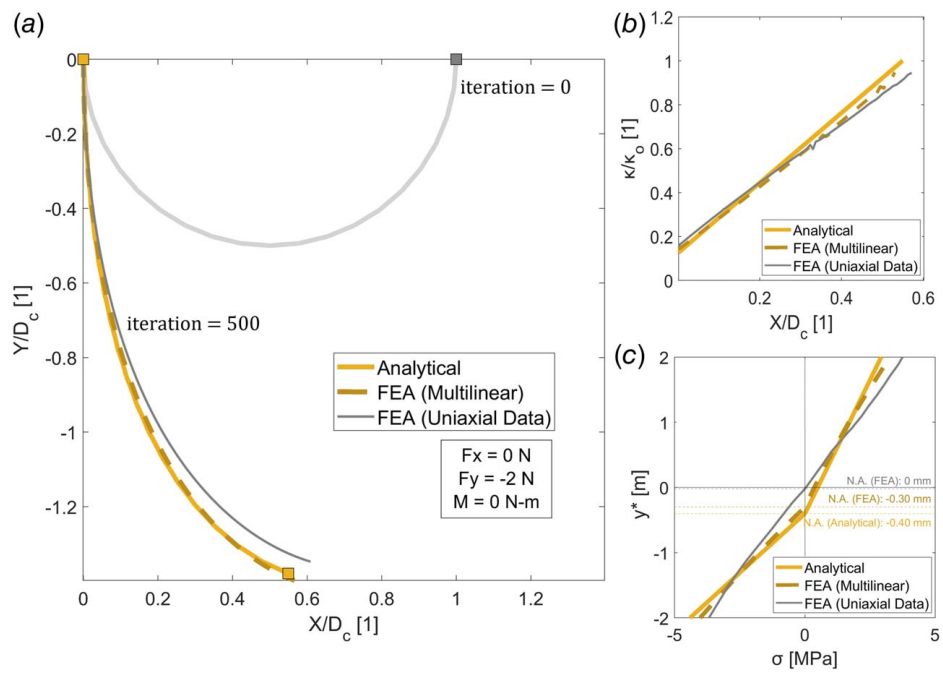
Fig. 14 Deflection profile of the TPU analytical model subject to a transverse force of −2 N (a), curvature profile along the arc in its deformed position (b), and stress distribution and neutral axis position at the fixed end of the arc compared with FEA using the uniaxial and multilinear models (c)

3.3 Folding Compliant Mechanism With Thermoplastic Polyurethane. Finally, the segmented arc model is extended to the folding CM design by attaching the small flexures and the rightmost frame to the ends of the arc in Fig. 15. The model is normalized by the total horizontal distance between the fixed end and the free end ($L_{tot} = 65$ mm). Again, the arc is segmented into $n = 20$ segments and has the same geometric parameters given in Table 4. The folding CM is segmented into 28 total segments and the out-of-plane thickness (a) remains constant and the same as the semicircular arc.
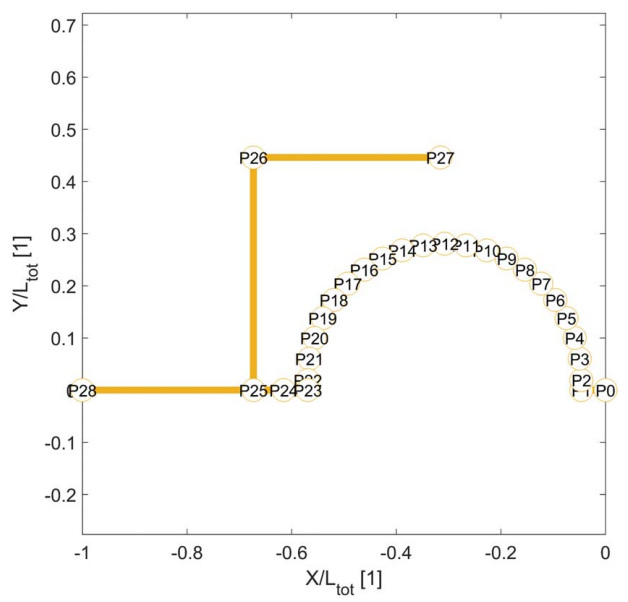

Fig. 15 Undeformed geometry of the segmented folding CM for $n = 25$ total segments, where the semicircular arc is segmented into $n = 20$ segments

A transverse force ($F_{y,\,max}$) of −0.5 N is applied to P28 instead of P20 in the semicircular arc model. The maximum strain attained is 50.5%. The final value of the weight used in the experimental study was 200 g or a magnitude of 1.96 N. However, due to the definition of the analytical model, only results up to a magnitude of 0.5 N can be obtained. This limitation is assumed to be due to the small strain assumption. For the previous NiTi beam and TPU arc examples, where the maximum strains were reported as 9.4% and 12.4%, respectively, it is possible that the strains are small relative to the geometries and nonlinear-elastic models studied. As mentioned for NiTi, 10% strain is considered a suitable threshold on the amount of recoverable strain. Since 9.4% strain is within this limit, the strain could be considered small. The material model for TPU reaches almost 400% strain in Fig. 11, which when compared to the 12.4% and 50.5% strain achieved by the arc and folding CM models could also indicate that the analytical model is more appropriate for small strains.

The deflection profile of the folding CM is then compared between the analytical model and FEA using the uniaxial data for TPU. The number of load steps remains $N_{iter} = 500$ for both models. While the two deflection curves agree toward the fixed end of the folding CM in Fig. 16, there is less overlap toward the location of the force.

The culmination of this work is to predict the behavior of an additively manufactured folding CM made from a nonlinear-elastic material. Given that the folding CM is an extension of the semicircular arc, and the arc is an extension of the cantilever beam through segmentation, validation of the folding CM experimentally would also validate the behavior of the primitive geometries. TPU filament was selected because it is more accessible and less costly than additively manufactured NiTi. Thus, an experimental study was performed to measure the deflection of three TPU specimens, which were averaged and plotted with +/− two standard deviation bands. As illustrated in Fig. 17, the experimental and FEA deflection curves of the two tracked points (A, B, C) up to a final force of 1.96 N demonstrate good agreement along the path of point C. All the points lie with the standard deviation band despite some slight differences in where the points fall along the path.
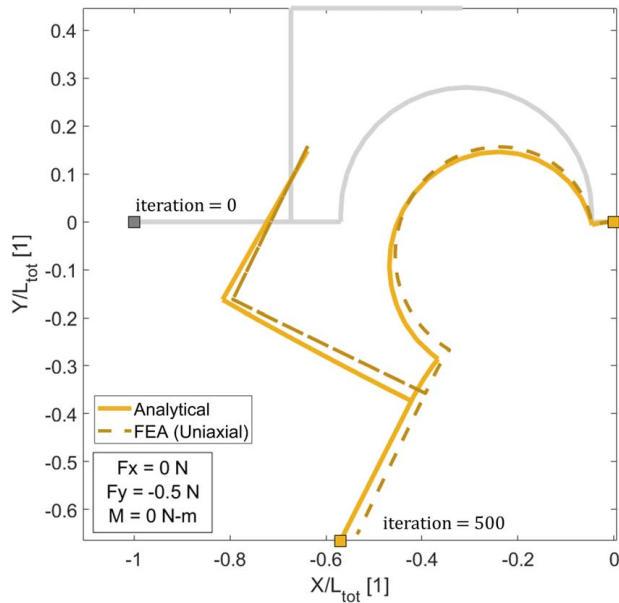
Fig. 16 Deflection profile of the TPU analytical model of the folding CM, subject to a transverse force of −0.5 N, illustrating the differences in the predicted deflection compared to FEA

Alternatively, the path of point B shows a greater deviation outside of the standard deviation band with an increasing applied force. These trends are also seen when the deflection of the analytical model is evaluated against the experiment.

For the analytical model, the initial positions of points B and C are determined from the original computer-aided design model of the folding CM design. Coordinate transformation was used to calculate the position of points B and C relative to the nearest segment tip position as it deforms. In this example, point B is calculated with respect to P27 and point C to P25 in Fig. 15. Since point A is assumed to be fixed, its position is set to the origin in the
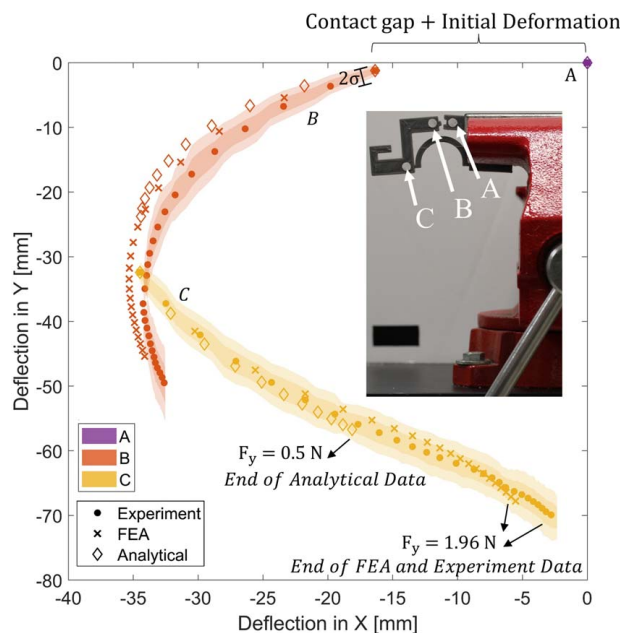

Fig. 17 Deflection path of points A, B, and C for the experiment, FEA, and analytical model, with shading indicating +/− two standard deviation bands (±2σ). The FEA and experimental data go up to a force of −1.96 N while the analytical data go up to −0.5 N.

Fig. 18 Illustration of the original location of the applied force at the tip of the folding CM and its shift caused by the increase in weight

experimental study or (0, 0). The points are then adjusted to match the orientation used in the experiment, accounting for the contact gap and initial deformation of the CM due to gravity. Yet, the model deviates from the experimental results along the path of point B similar to the FEA model. This observation is possibly explained by a small shift in the location of the applied force in the experiment. As seen in Fig. 18, the folding CM was designed with a hook attachment to suspend the weights at its tip. As the weight increases, the original location of the hanging weight shifts inside of the hook attachment. It is possible that the paths of the FEA and analytical models move away from the experimental solution because of this shift. The slight change in the applied force location could create an additional moment that impacts the deflection path. Since the moment arm from the force to point B is larger than that to point C, the deviation from the experimental results along the path of point B is more noticeable.

Additional possible sources of error include human error in capturing the images of the folding CM, local deformations of the CM, and time-dependent properties such as creep and stress relaxation that would cause permanent deformation during loading and unloading. In terms of comparing the analytical and FEA models to the experiment, the assumption of a zero Poisson's ratio also may not be suitable for the true behavior of the material, since TPU has a Poisson's ratio that can be as high as 0.48–0.5 [49,50]. However, this assumption does allow for the creation of a fast analytical model for 1D problems. The analytical model is shown to reasonably predict the behavior of an additively manufactured CM made from TPU within the range of forces applied. The versatility of the developed model for nonlinear-elastic materials is reflected in the good agreement in the results for both a material with less pronounced tension–compression asymmetry (NiTi) and one with more pronounced asymmetry (TPU), even with the additional complexity of large deformations and nonuniform geometries.

4 Conclusions

To understand the behavior of CMs with nonlinear-elastic materials, an analytical model including tension–compression asymmetry is considered. The main contributions of this work include: (1) constitutive equations for unifying geometric and material nonlinearity in a cantilever beam, (2) a segmentation approach for a semicircular arc and folding CM, (3) a generalized multilinear model for nonlinear-elastic materials with asymmetric mechanical properties applied to NiTi and TPU, and (4) experimental and FEA-based

validation of the analytical model for an additively manufactured folding CM from TPU.

The limit on convergence of the model indicates a maximum achievable strain that still needs to be studied further. The limitation is assumed to be due to the definition of the strain, using the von Kármán strain theory, which does not include the higher order strain terms of the finite strain theory. The value of the maximum strain prior to nonconvergence also depends on the geometry and possibly the material. Thus, a correlation between the strain and the bending stiffness, or flexural rigidity (EI), of the model also needs to be determined to quantify the limit on the strain using this approach.

Continued research in the area of CM models aims to explore the fabrication of shape morphing structures. Designs such as the folding CM could be incorporated as compliant joints in origami-based mechanisms. Another iteration of the analytical model, accounting for the self-contact mechanism of the folding CM, would serve to tap into the energy absorption and stress-relief properties of cellular contact-aided compliant mechanisms. The response of the contact mechanism could theoretically be represented by a nonlinear translational spring in future work.

Lastly, with the ability to model nonlinear-elastic materials with tension–compression asymmetry, experimental data for other materials used in AM could also be used to validate the accuracy of the analytical model. These studies can then be expanded to not only predict the nonlinear behavior of different additively manufactured CM geometries but also tailor their geometry and functionality through design optimization.

Acknowledgment

Conflict of Interest

The authors declare that they have no known competing financial interests or personal relationships that could have appeared to influence the work reported in this paper.

Data Availability Statement

The datasets generated and supporting the findings of this article are obtainable from the corresponding author upon reasonable request.

Nomenclature

a = out-of-plane thickness of cross section
b = in-plane half thickness of cross section
i = index of beam element tip position
j = index of segment tip position
k = linear section of the multilinear material model
n = number of segments
s = arc length
F = internal force due to bending along beam
L = undeformed length of the cantilever beam
M = internal moment due to bending along beam
N = internal force due to axial stretching along beam
V = internal force due to shear along beam
L_s = length of segment
M_o = applied tip moment
N_{iter} = number of iterations for the analytical model
N_p = number of discretization points for beam elements
P_j = global tip position of segments
R_c = radius of arc with respect to centroidal axis
R_o = initial radius of curvature
y^* = position along beam thickness in y

y^* = shift of neutral axis from centroidal axis of beam
$E_k^{(t,c)}$ = elastic modulus for linear section k
M_j^{eq} = equivalent applied moment for the segmented model
l, l_o = projected length of beam, initially straight or curved
m, m_o = tip deflection of beam, initially straight or curved
u, v = axial and transverse deflections along centroidal axis
x, y = local coordinates of displacement
$y_1^{(t,c)*}, y_2^{(t,c)*}$ = critical y^* transition points
F_x, F_y = applied non-follower tip loads
X, Y = global coordinates of displacement
α = sector angle of arc
β_j = subtended angle of arc
$\varepsilon, \varepsilon_b, \varepsilon_m$ = strain with bending and membrane components
$\varepsilon_1^{(t,c)}, \varepsilon_2^{(t,c)}$ = critical strains in tension and compression
$\varepsilon_{res}^{(t,c)}$ = residual strains in tension and compression
ζ_j = initial angle of rotation for segment
θ = slope or angle of deflection along beam
κ, κ_o = curvature due to bending and initial curvature
$\kappa_1^{(t,c)}, \kappa_2^{(t,c)}$ = critical curvatures
$\sigma_k^{(t,c)}$ = uniaxial stress for linear section k
$\sigma_1^{(t,c)*}, \sigma_2^{(t,c)*}$ = critical stresses in tension and compression
ψ = central angle of arc

References

[1] Jovanova, J., Nastevska, A., and Frecker, M., 2019, "Tailoring Energy Absorption With Functional Grading of a Contact-Aided Compliant Mechanism," Smart Mater. Struct., **28**(8), p. 084003.
[2] Pernette, E., Henein, S., Magnani, I., and Clavel, R., 1997, "Design of Parallel Robots in Microrobotics," Robotica, **15**(4), pp. 417–420.
[3] Saggere, L., and Kota, S., 1999, "Static Shape Control of Smart Structures Using Compliant Mechanisms," AIAA J., **37**(5), pp. 572–578.
[4] Kota, S., Joo, J., Li, Z., Rodgers, S. M., and Sniegowski, J., 2001, "Design of Compliant Mechanisms: Applications to MEMS," Analog Integr. Circuits Signal Process., **29**(1/2), pp. 7–15.
[5] Speich, J., and Goldfarb, M., 2000, "A Compliant-Mechanism-Based Three Degree-of-Freedom Manipulator for Small-Scale Manipulation," Robotica, **18**(1), pp. 95–104.
[6] Frecker, M. I., Ananthasuresh, G. K., Nishiwaki, S., Kikuchi, N., and Kota, S., 1997, "Topological Synthesis of Compliant Mechanisms Using Multi-criteria Optimization," ASME J. Mech. Des., **119**(2), pp. 238–245.
[7] Howell, L. L., and Midha, A., 1994, "A Method for the Design of Compliant Mechanisms With Small-Length Flexural Pivots," ASME J. Mech. Des., **116**(1), pp. 280–290.
[8] Moon, Y.-M., Trease, B. P., and Kota, S., 2002, "Design of Large-Displacement Compliant Joints," Proceedings of the ASME 2002 International Design Engineering Technical Conferences and Computers and Information in Engineering Conference. Volume 5: 27th Biennial Mechanisms and Robotics Conference, ASME, Montreal, Quebec, Canada, Sept. 29–Oct. 2, ASME, Vol. 5, pp. 65–76.
[9] Ahuett-Garza, H., Chaides, O., Garcia, P. N., and Urbina, P., 2014, "Studies About the Use of Semicircular Beams as Hinges in Large Deflection Planar Compliant Mechanisms," Precis. Eng., **38**(4), pp. 711–727.
[10] Saxena, A., and Kramer, S. N., 1998, "A Simple and Accurate Method for Determining Large Deflections in Compliant Mechanisms Subjected to End Forces and Moments," ASME J. Mech. Des., **120**(3), pp. 392–400.
[11] Howell, L. L., 2001, Compliant Mechanisms, 1st ed., John Wiley & Sons, Inc., New York.
[12] Pedersen, C. B. W., Buhl, T., and Sigmund, O., 2001, "Topology Synthesis of Large-Displacement Compliant Mechanisms," Int. J. Numer. Methods Eng., **50**(12), pp. 2683–2705.
[13] Kumar, P., Saxena, A., and Sauer, R. A., 2019, "Computational Synthesis of Large Deformation Compliant Mechanisms Undergoing Self and Mutual Contact," ASME J. Mech. Des., **141**(1), p. 012302.
[14] Saxena, A., 2005, "Topology Design of Large Displacement Compliant Mechanisms With Multiple Materials and Multiple Output Ports," Struct. Multidiscipl. Optim., **30**(6), pp. 477–490.
[15] Zeng, X., Hurd, C., Su, H.-J., Song, S., and Wang, J., 2020, "A Parallel-Guided Compliant Mechanism With Variable Stiffness Based on Layer Jamming," Mech. Mach. Theory, **148**, p. 103791.
[16] Najmon, J. C., Dehart, J., Wood, Z., and Tovar, A., 2018, "Cellular Helmet Liner Design Through Bio-inspired Structures and Topology Optimization of Compliant Mechanism Lattices," SAE Int. J. Transp. Saf., **6**(3), pp. 217–235.
[17] Kumar, P., Sauer, R. A., and Saxena, A., 2021, "On Topology Optimization of Large Deformation Contact-Aided Shape Morphing Compliant Mechanisms," Mech. Mach. Theory, **156**, p. 104135.

[18] Liu, L., Xing, J., Yang, Q., and Luo, Y., 2017, "Design of Large-Displacement Compliant Mechanisms by Topology Optimization Incorporating Modified Additive Hyperelasticity Technique," Math. Probl. Eng., **2017**, p. 4679746.

[19] Bruns, T. E., and Tortorelli, D. A., 2001, "Topology Optimization of Non-linear Elastic Structures and Compliant Mechanisms," Comput. Methods Appl. Mech. Eng., **190**(26–27), pp. 3443–3459.

[20] Howell, L. L., and Midha, A., 1995, "Parametric Deflection Approximations for End-Loaded, Large-Deflection Beams in Compliant Mechanisms," ASME J. Mech. Des., **117**(1), pp. 156–165.

[21] Venkiteswaran, V. K., and Su, H. J., 2016, "Pseudo-Rigid-Body Models for Circular Beams Under Combined Tip Loads," Mech. Mach. Theory, **106**, pp. 80–93.

[22] Zirbel, S. A., Tolman, K. A., Trease, B. P., and Howell, L. L., 2016, "Bistable Mechanisms for Space Applications," PLoS One, **11**(12), p. e0168218.

[23] Hargrove, B., Nastevska, A., Frecker, M., and Jovanova, J., 2022, "Pseudo Rigid Body Model for a Nonlinear Folding Compliant Mechanism," Mech. Mach. Theory, **176**, p. 105017.

[24] Jin, M., Zhu, B., Mo, J., Yang, Z., Zhang, X., and Howell, L. L., 2020, "A CPRBM-Based Method for Large-Deflection Analysis of Contact-Aided Compliant Mechanisms Considering Beam-to-Beam Contacts," Mech. Mach. Theory, **145**, p. 103700.

[25] Banerjee, A., Bhattacharya, B., and Mallik, A. K., 2008, "Large Deflection of Cantilever Beams With Geometric Non-linearity: Analytical and Numerical Approaches," Int. J. Non Linear Mech., **43**(5), pp. 366–376.

[26] Chen, G., Ma, F., Hao, G., and Zhu, W., 2019, "Modeling Large Deflections of Initially Curved Beams in Compliant Mechanisms Using Chained Beam Constraint Model," ASME J. Mech. Rob., **11**(1), p. 011002.

[27] Jeong, S., and Yoo, H. H., 2017, "Flexibility Modeling of a Beam Undergoing Large Deflection Using the Assumed Mode Method," Int. J. Mech. Sci., **133**, pp. 611–618.

[28] Tsiatas, G. C., and Babouskos, N. G., 2017, "Linear and Geometrically Nonlinear Analysis of Non-uniform Shallow Arches Under a Central Concentrated Force," Int. J. Non Linear Mech., **92**, pp. 92–101.

[29] Li, D. K., and Li, X. F., 2016, "Large Deflection and Rotation of Timoshenko Beams With Frictional End Supports Under Three-Point Bending," C. R. Méch., **344**(8), pp. 556–568.

[30] Shvartsman, B. S., 2013, "Analysis of Large Deflections of a Curved Cantilever Subjected to a Tip-Concentrated Follower Force," Int. J. Non Linear Mech., **50**, pp. 75–80.

[31] Mohyeddin, A., and Fereidoon, A., 2014, "An Analytical Solution for the Large Deflection Problem of Timoshenko Beams Under Three-Point Bending," Int. J. Mech. Sci., **78**, pp. 135–139.

[32] Eshghinejad, A., and Elahinia, M., 2015, "Exact Solution for Bending of Shape Memory Alloy Beams," Mech. Adv. Mater. Struct., **22**(10), pp. 829–838.

[33] Auricchio, F., Taylor, R. L., and Lubliner, J., 1997, "Shape-Memory Alloys: Macromodelling and Numerical Simulations of the Superelastic Behavior," Comput. Methods Appl. Mech. Eng., **146**(3–4), pp. 281–312.

[34] Hargrove, B., Nastevska, A., Jovanova, J., and Frecker, M., 2021, "Shape Memory Modeling of a Nonlinear and Superelastic Compliant Mechanism,"

[35] Chen, L., 2010, "An Integral Approach for Large Deflection Cantilever Beams," Int. J. Non Linear Mech., **45**(3), pp. 301–305.

[36] Ghuku, S., and Nath Saha, K., 2016, "A Theoretical and Experimental Study on Geometric Nonlinearity of Initially Curved Cantilever Beams," Eng. Sci. Technol. Int. J., **19**(1), pp. 135–146.

[37] Van Viet, N., Zaki, W., and Umer, R., 2018, "Analytical Model for a Superelastic Timoshenko Shape Memory Alloy Beam Subjected to a Loading–Unloading Cycle," J. Intell. Mater. Syst. Struct., **29**(20), pp. 3902–3922.

[38] Van Viet, N., Zaki, W., and Moumni, Z., 2019, "A Model for Shape Memory Alloy Beams Accounting for Tensile Compressive Asymmetry," J. Intell. Mater. Syst. Struct., **30**(18–19), pp. 18–19.

[39] Nastevska, A., Jovanova, J., and Frecker, M., 2020, "Design of Compliant Joints for Large Scale Structures," ASME 2020 Conference on Smart Materials, Adaptive Structures and Intelligent Systems, Virtual, Online, Sept. 15, pp. 1–10.

[40] Rajagopal, K. R., 2014, "On the Nonlinear Elastic Response of Bodies in the Small Strain Range," Acta Mech., **225**(6), pp. 1545–1553.

[41] Janečka, A., Průša, V., and Rajagopal, K. R., 2016, "Euler–Bernoulli Type Beam Theory for Elastic Bodies With Nonlinear Response in the Small Strain Range," Arch. Mech., **68**(1), pp. 3–25.

[42] Khodabakhshi, P., and Reddy, J. N., 2017, "A Unified Beam Theory With Strain Gradient Effect and the von Kármán Nonlinearity," Z. Angew. Math. Mech., **97**(1), pp. 70–91.

[43] Reddy, J. N., and Mahaffey, P., 2013, "Generalized Beam Theories Accounting for von Kármán Nonlinear Strains With Application to Buckling," J. Coupled Syst. Multiscale Dyn., **1**(1), pp. 120–134.

[44] Altenbach, H., Belyaev, A., and Palmov, V. A., 2020, "Plate Theory After von Kármán," Encyclopedia of Continuum Mechanics, 1st ed., Springer, Berlin, Heidelberg, pp. 2068–2076.

[45] Naghdi, P. M., and Vongsarnpigoon, L., 1983, "A Theory of Shells With Small Strain Accompanied by Moderate Rotation," Arch. Ration Mech. Anal., **83**(3), pp. 245–283.

[46] Desai, S. M., Sonawane, R. Y., and More, A. P., 2023, "Thermoplastic Polyurethane for Three-Dimensional Printing Applications: A Review," Polym. Adv. Technol., **34**(7), pp. 2061–2082.

[47] Płatek, P., Rajkowski, K., Cieplak, K., Sarzyński, M., Małachowski, J., Woźniak, R., and Janiszewski, J., 2020, "Deformation Process of 3D Printed Structures Made From Flexible Material With Different Values of Relative Density," Polymers, **12**(9), p. 2120.

[48] Robertson, S. W., Pelton, A. R., and Ritchie, R. O., 2013, "Mechanical Fatigue and Fracture of Nitinol," Int. Mater. Rev., **57**(1), pp. 1–36.

[49] Qi, H. J., and Boyce, M. C., 2005, "Stress–Strain Behavior of Thermoplastic Polyurethanes," Mech. Mater., **37**(8), pp. 817–839.

[50] Pham, N. K., and Peraza Hernandez, E. A., 2021, "Modeling and Design Exploration of a Tensegrity-Based Twisting Wing," ASME J. Mech. Rob., **13**(3), p. 031019.

ASME 2021 Conference on Smart Materials, Adaptive Structures and Intelligent Systems, Virtual, Online, Sept. 14–15.